



Rethinking Pulmonary Nodule Detection in Multi-view 3D CT Point Cloud Representation

Jingya Liu¹, Oguz Akin², and Yingli Tian¹(✉)

¹ The City College of New York, New York, NY 10031, USA
ytian@ccny.cuny.edu

² Memorial Sloan Kettering Cancer Center, New York, NY 10065, USA

Abstract. 3D CT point clouds reconstructed from the original CT images are naturally represented in real-world coordinates. Compared with CT images, 3D CT point clouds contain invariant geometric features with irregular spatial distributions from multiple viewpoints. This paper rethinks pulmonary nodule detection in CT point cloud representations. We first extract the multi-view features from a sparse convolutional (SparseConv) encoder by rotating the point clouds with different angles in the world coordinate. Then, to simultaneously learn the discriminative and robust spatial features from various viewpoints, a nodule proposal optimization schema is proposed to obtain coarse nodule regions by aggregating consistent nodule proposals prediction from multi-view features. Last, the multi-level features and semantic segmentation features extracted from a SparseConv decoder are concatenated with multi-view features for final nodule region regression. Experiments on the benchmark dataset (LUNA16) demonstrate the feasibility of applying CT point clouds in lung nodule detection task. Furthermore, we observe that by combining multi-view predictions, the performance of the proposed framework is greatly improved compared to single-view, while the interior texture features of nodules from images are more suitable for detecting nodules in small sizes.

Keywords: 3D point cloud · Nodule detection · Multi-view feature representation

1 Introduction

Lung cancer is the leading cancer killer and one of the most common cancers around the world [26]. Many efforts have been made on AI-driven computer-aided diagnosis (CAD) systems for lung nodule detection and diagnosis [17, 18, 28, 31]. Most existing 3D nodule detectors [11, 31] extract spatial-temporal features from the stacked CT images as 3D volumes via 3D convolutional neural networks (3D CNNs). By extending a two-dimensional feature representation to a three-dimensional space, the significant performance improvement demonstrates the

benefits of interpreting the spatial features for nodule detection. Meanwhile, by projecting CT images to multiple planes (i.e., axial, coronal, and sagittal), the multi-view features show the effectiveness to reduce false positives as richer features are obtained from different viewpoints [9, 16, 22, 23]. Although these existing methods can extract spatial-temporal features or multi-view features from the continuous CT images, the data representation with multi-view flexibility that can directly represent 3D spatial features is still remain exploring.

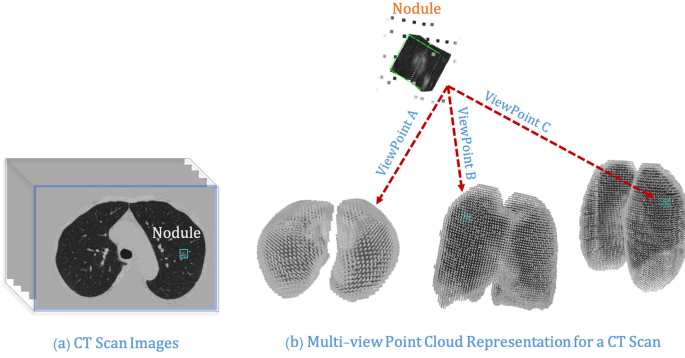


Fig. 1. Illustration of a CT scan in the image (a) and CT point cloud visualized in different views (b). Compared to CT images, as shown in (b), 3D CT point clouds naturally represent pulmonary nodules by multi-view representations in 3D coordinates. View A in (b) has the same viewpoint as the CT image. Note that the background of the lung region is excluded for both CT images and CT point clouds. Best viewed in color.)

Table 1. Comparison between CT image representation and 3D CT point cloud representations.

| Visual representation | Geometric invariance | Multi-view perspective | Real-world coordinates | Irregular shape | Grid align | Texture feature | Radiation intensity |
|-----------------------|----------------------|------------------------|------------------------|-----------------|------------|-----------------|---------------------|
| Image | No | No | No | No | Yes | Yes | Yes |
| 3D point cloud | Yes | Yes | Yes | Yes | No | No | Yes |

Recently, 3D point clouds are considered to be a natural way to capture and represent 3D objects [2, 4, 12, 20, 21]. As shown in Fig. 1, unlike CT images (Fig. 1(a)) represented by grids, 3D CT point clouds (Fig. 1(b)) are organized in an irregular manner, thereby provides more flexible feature representations of 3D geometric structure. We summarize the characters of visual representations of 3D CT point clouds and CT images in Table 1. Real-world coordinates are applied to 3D CT point clouds, representing the accurate geometric distribution of radiation intensity. Due to geometric invariance, multi-view representations can be obtained by tilting the 3D CT point cloud heading angles to obtain richer

features than the single-view representation. However, the scattered 3D CT point cloud lacks the texture features as CT images that preserve the details of internal nodules. Therefore, this paper attempts to rethink the nodule detection task from multiple perspectives in CT point clouds and investigate the advantages and limitations compared to CT images.

Existing models that apply 3D point clouds to medical image analysis mainly in small areas, such as intra-oral scans [30] and cropped nodule candidate regions [8]. We aim to address the challenging task of predicting nodule regions in the entire lung area. Per our knowledge, this is the first work to explore 3D point cloud data representation for the nodule detection task. The main contributions of this paper are summarized as follows: 1) We explore the possibility of applying 3D CT point cloud and the effectiveness of 3D spatial representations on nodule detection. By rotating the 3D CT point clouds, compared to a single view of stacked CT images, irregular shapes and richer spatial distributions of nodules in lung regions are extracted from multi-views. 2) A nodule proposal optimization schema is proposed to acquire a set of 3D nodule candidate proposals which simultaneously agreed by multi-view feature predictions. The rich multi-level features and point-wise segmentation are further concatenated with multi-view features for final nodule candidate refinement. 3) Experiment results show the advantages of multi-view 3D CT point clouds as spatial representations and the impact of lacking the texture feature representations on small nodule detection. Furthermore, the ablation studies demonstrate that with more multi-views involved, the performance of the proposed framework achieves encouraging improvements, proofing the effectiveness of multi-view 3D features in point clouds.

2 Methods

As shown in Fig. 2, N samples are acquired by combining the original 3D CT point clouds with the rotated multi-view samples, representing irregular geometric distributions from various perspectives. A 3D Sparse Convolution (SparseConv) encoder simultaneously learns the multi-view features by optimizing the nodule proposals in various viewpoints. Last, a final nodule prediction is refined by fusing the multi-level features and semantic segmentation features extracted by the 3D SparseConv decoder, as well as the multi-view features.

Multi-view Sample Collection: 3D CT point clouds consist of a set of three-dimensional vertices, defined as $\{x, y, z\}$ representing the distribution of points in a world coordinate. Besides, the unique internal texture with the radiation intensities is essential to identify nodule types. We further apply the radiant intensity I of each point to preserve internal intensity-based texture features. The nodule region is represented by (x, y, z, h, w, l) , indicating the nodule location $\{x, y, z\}$ and the nodule size in three dimensions $\{h, w, l\}$. During the training, the objective function consists of the BinaryCrossEntropy loss for nodule class probability and *smooth-l1* loss for nodule region by comparing the predicted nodule candidates and the ground-truths.

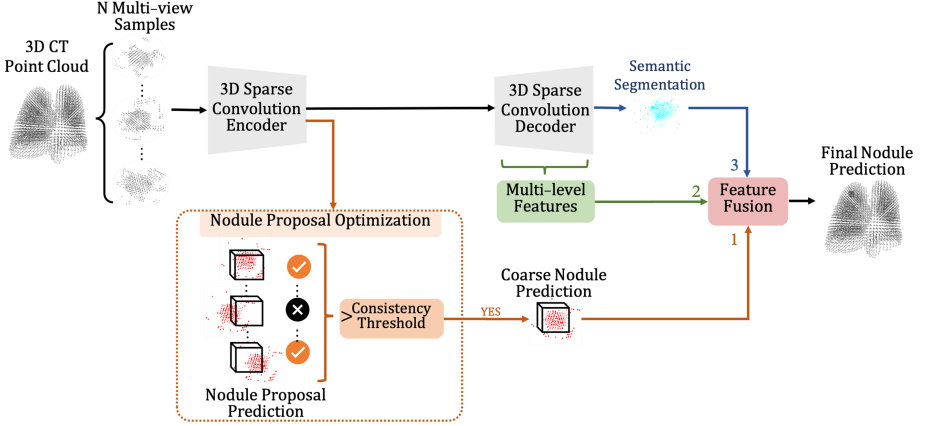


Fig. 2. The pipeline of our proposed 3D point cloud nodule detection framework. Multi-view feature representations are extracted from a 3D sparse encoder-decoder network and further employed to select the coarse nodule predictions by a nodule proposal optimization (details are illustrated in Fig. 3 and explained in Sect. 3 - Nodule Proposal Optimization). Then, the finer candidate prediction is obtained based on the fusion of 1) multi-view features; 2) multi-level features; 3) semantic features of the region of interest (ROI).

By rotating the 3D point clouds along the world coordinate in N angles, the discriminate multi-view features of the same object can be extracted. Therefore, to train a backbone network with robust spatial features from multiple perspectives, we rotate the 3D CT point clouds along the xy -axis, yz -axis, xz -axis, and xyz -axis with a set of rotation angles from $+\theta$ to $-\theta$. As shown in Fig. 3, four sets of $(N - 1)$ viewpoints are added, donated as V - xy , V - yz , V - xz , and V - xyz . We implement nine viewpoint samples with the rotation angles of $+45^\circ$ and -45° for V - xy , V - yz , V - xz , and V - xyz . The multi-view features are fed into the backbone network for nodule proposal prediction.

Multi-view and Multi-level Feature Extraction: The irregular shape of the 3D point cloud brings challenges to implement feature extraction with convolutional neural networks (CNN). We follow the baseline PV-RCNN [24] and the extension work, Part-A² [25] to extract features by integrating the grids of irregular point clouds as voxels and multi-level point-wise features from the decoder network. A 3D sparse convolution (SparseConv) encoder composed of four layers as es_1 , es_2 , es_3 , and es_4 . The features are downsampled to $1 \times$, $2 \times$, $4 \times$, $8 \times$ as the layers go deeper. A 3D SparseConv decoder comprises four sparse deconvolutional layers as ds_1 , ds_2 , ds_3 , and ds_4 for feature upsampling. The lateral connections are conducted through all layers, as the es_1 with ds_1 , es_2 with ds_2 , es_3 with ds_3 , and es_4 with ds_4 , extracting the multi-level point-wise features for final candidate prediction.

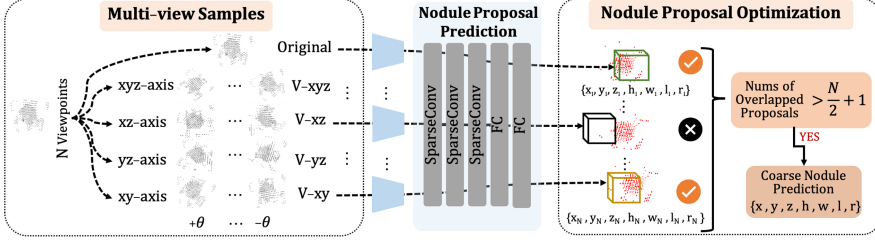


Fig. 3. The detailed illustration of the proposed multi-view samples and nodule prediction optimization schema. Multi-view samples are obtained by rotating the original samples from N viewpoints. By rotating from $+\theta$ to $-\theta$ along the xy -axis, yz -axis, xz -axis, and xyz -axis, $(N - 1)$ additional viewpoints are obtained as V - xy , V - yz , V - xz and V - xyz . Features of N views are extracted from the 3D SparseConv encoder and the primary nodule proposals are predicted by a regression head. The coarse nodule predictions are collected if the number of consensus nodule proposals predicted by the multi-view features is greater than a consistency threshold.

Nodule Proposal Optimization: Unlike typical data augmentation methods, we employ the samples from all views to predict and optimize the nodule proposals simultaneously. Reliable preliminary nodule proposals are acquired from multi-views. In the meantime, compared with the ground truth, the 3D SparseConv encoder is updated by the objective function to extract multi-view features for accurate predictions. The distinguish and robust features ensure the prediction of the nodule regions. As shown in Fig. 3, a regression head (RH) is used for nodule proposal prediction, which consists of three SparseConv layers, followed by two fully connected layers to predict the confidence score and proposal region. RH takes the features of N views extracted from the last SparseConv layer of the encoder network and predicts the initial coarse nodule candidate regions. First, we choose a nodule proposal with a confidence score greater than 0.05 and then calculate the number of nodule proposals with a 3D IoU of 0.25 overlap among the multi-view predictions. If the number is higher than a consistency threshold, the nodule proposal is set as the coarse nodule prediction for a finer region regression.

Final Nodule Prediction with Multi-feature Fusion: To guarantee an accurate nodule candidate prediction, rich feature fusion is conducted by combining the multi-view features, multi-level features, and semantic segmentation features, as shown in Fig. 2. First, the point-wise attention benefits the flexible receptive field from the irregular format. We follow PV-RCNN [24], multi-scale features are extracted from $ds1$, $ds2$, $ds3$, and $ds4$ layers. Second, semantic segmentation maps are predicted by the 3D decoder network and semantic features further extracted by a SparseConv, interpreting the point level classification of nodule candidates. Finally, same as Part-A² [25], the multi-level features and the semantic features are concatenated for nodule region prediction along with

the multi-view features. A regression head predicts the final nodule candidate region (x, y, z, h, w, l, r) based on the rich multi-feature fusion.

3 Experiments

3.1 Data and Training

We conduct the experiments on the LUNA16 public dataset [1], which contains 1,186 nodules with sizes ranging from 3 to 30 mm from 888 CT scans. The dataset is officially divided into ten subsets. We follow the same cross-validation protocol by applying nine subsets as training and the remaining subset as testing. One subset from the training subsets is used for validation to monitor the convergence of the training process.

3D CT Point Cloud Reconstruction: A CT scan consists of CT images represented by (x, y) as image coordinates and z as scan depth. To eliminate unrelated regions, we first segment the lung region from the CT images based on the lung region mask and then apply (x, y, z) as the location of each point in the world coordinates, represented by $(x, y, z, \text{radiation intensity})$. The air points in the lung regions are discarded based on the standard Hounsfield scale (-1000). Therefore, the CT point clouds precisely represent the nodules, tissues, organs, and lung boundaries in the lung region. Besides, to avoid sampling redundant and non-informative points in the training, we follow Drokin *et al.* [8] by applying the non-uniform sampling schema, which keeps a high sampling rate at the nodule regions and gradually reduces the sampling rate according to the increasing distance from sample points to the center of nodules.

Model Training: The experiment is modified based on an open source project OpenPCDet [27]. The proposed framework is trained to minimize BinaryCrossEntropy loss and *Smooth-L1* loss. The Adam algorithm is used for optimization with an initial learning rate of $1e^{-4}$ and decreased by 0.1 after 80 and 160 epochs. The batch size is set to 2. The multi-view proposal optimization is conducted after 20 epochs. The model is trained with a total of 200 training epochs.

3.2 Experiments on LUNA16

Compare with State-of-the-Art Nodule Detection Methods: We evaluate the proposed method and compare it with the state-of-the-art image-based nodule detectors in two groups: one-stage methods without false-positive reduction and two-stage frameworks with false-positive reduction. Similar to the LUNA16 challenge, the Free-Response ROC Curve (FROC) [3] is employed to evaluate the sensitivity versus the specificity of the nodule detection at 1/8, 1/4, 1/2, 1, 2, 4, 8 False Positive (FP) levels per scan with the average Competition Performance Metric (CPM) score. As shown in Table 2, the proposed 3D nodule detector reaches comparable results with the one-stage methods trained

Table 2. FROC performance comparison of nodule detection between the proposed 3D point cloud-based method and the state-of-the-art image-based methods on LUNA16 dataset: sensitivity and the corresponding false positives at 1/8, 1/4, 1/2, 1, 2, 4, 8 per scan with and without false positive reduction.

| Methods | 1/8 | 1/4 | 1/2 | 1 | 2 | 4 | 8 | CPM |
|----------------------------------|-------|-------|-------|-------|-------|-------|-------|-------|
| Without false positive reduction | | | | | | | | |
| Zhu <i>et al.</i> [31] | 0.692 | 0.769 | 0.824 | 0.865 | 0.893 | 0.917 | 0.933 | 0.842 |
| Li <i>et al.</i> [15] | 0.739 | 0.803 | 0.858 | 0.888 | 0.907 | 0.916 | 0.920 | 0.862 |
| Gong <i>et al.</i> [10] | 0.713 | 0.801 | 0.867 | 0.917 | 0.920 | 0.962 | 0.971 | 0.883 |
| Khosravan <i>et al.</i> [13] | 0.709 | 0.836 | 0.921 | 0.953 | 0.953 | 0.953 | 0.953 | 0.897 |
| Liu <i>et al.</i> [17] | 0.848 | 0.876 | 0.905 | 0.933 | 0.943 | 0.957 | 0.970 | 0.919 |
| With false positive reduction | | | | | | | | |
| Dou <i>et al.</i> [7] | 0.677 | 0.737 | 0.815 | 0.848 | 0.879 | 0.907 | 0.922 | 0.827 |
| Dou <i>et al.</i> [6] | 0.659 | 0.745 | 0.819 | 0.865 | 0.906 | 0.933 | 0.946 | 0.839 |
| Wang <i>et al.</i> [29] | 0.676 | 0.776 | 0.879 | 0.949 | 0.958 | 0.958 | 0.958 | 0.878 |
| Ding <i>et al.</i> [5] | 0.748 | 0.853 | 0.887 | 0.922 | 0.938 | 0.944 | 0.946 | 0.891 |
| Kim <i>et al.</i> [14] | 0.904 | 0.931 | 0.943 | 0.947 | 0.952 | 0.956 | 0.962 | 0.942 |
| Ours | 0.779 | 0.848 | 0.914 | 0.918 | 0.939 | 0.939 | 0.939 | 0.895 |
| Ours (w/FPR) | 0.794 | 0.886 | 0.916 | 0.934 | 0.951 | 0.956 | 0.959 | 0.913 |

on stacked CT images, demonstrating that the spatial features are feasible to employ in the nodule detection task. We observe that performance is improved with a small margin (1.6% CPM) by implementing the false positive reduction to the proposed nodule detector and shows a comparable result with the image-based two-stage frameworks [5–7, 29]. We notice that most of the missing nodules are small, with an average size of 5 mm. With few point representations, spatial feature extraction is significantly limited for all the SparseConv encoder layers. For the image-based methods, detailed internal texture features of small nodules are better preserved by the feature pyramid extraction [17, 29].

Ablation Study: We investigate the effectiveness of the proposed multi-view feature learning with the nodule proposal optimization schema and the feature fusion on the final nodule candidate predictions. For all ablation studies, the consistency threshold is set to 5 when 9 views involved as the model shows the best performance. Table 3 shows that the CPM is increased by 11.7% when all viewpoints are applied compared with the single-view baseline. As the multi-view features V-xy, V-yz, V-xz, and V-xyz gradually join for training, the sensitivities are raised by 3%, 4.4%, 3.2%, and 1.1% CPM, respectively. The performance is significantly gained by learning the multi-view feature representations through nodule proposal optimization schema. The average sensitivity is further improved 0.7% and 1.4% CPM by multi-level features (MF) and semantic feature (SF) for final nodule prediction, respectively, demonstrating the benefits of irregular

Table 3. Ablation study of the effectiveness of proposed multi-views samples with nodule proposal optimization, multi-level features (MF) and semantic features (SF) by comparing the performance on LUNA16 dataset: sensitivity and the corresponding false positives at 1/8, 1/4, 1/2, 1, 2, 4, 8 per scan.

| V-xy | V-yz | V-xz | V-xyz | MF | SF | 1/8 | 1/4 | 1/2 | 1 | 2 | 4 | 8 | CPM |
|------|------|------|-------|----|----|-------|-------|-------|-------|-------|-------|-------|-------|
| – | – | – | – | – | – | 0.617 | 0.695 | 0.765 | 0.796 | 0.811 | 0.811 | 0.811 | 0.758 |
| ✓ | – | – | – | – | – | 0.632 | 0.719 | 0.787 | 0.819 | 0.837 | 0.862 | 0.862 | 0.788 |
| ✓ | ✓ | – | – | – | – | 0.701 | 0.749 | 0.849 | 0.866 | 0.879 | 0.891 | 0.891 | 0.832 |
| ✓ | ✓ | ✓ | – | – | – | 0.742 | 0.801 | 0.863 | 0.904 | 0.907 | 0.917 | 0.917 | 0.864 |
| ✓ | ✓ | ✓ | ✓ | – | – | 0.756 | 0.835 | 0.879 | 0.902 | 0.911 | 0.921 | 0.921 | 0.875 |
| ✓ | ✓ | ✓ | ✓ | ✓ | – | 0.772 | 0.843 | 0.881 | 0.916 | 0.919 | 0.927 | 0.927 | 0.883 |
| ✓ | ✓ | ✓ | ✓ | ✓ | ✓ | 0.779 | 0.848 | 0.914 | 0.918 | 0.939 | 0.939 | 0.939 | 0.897 |

point-wise feature fusion for nodule region regression. We further compare the baseline model to the existing point cloud backbone networks: PointNet [20], PointNet++ [21] and DGCNN [19]. The PV-RCNN substantially outperforms these models by 4.2%, 3.3%, and 3.6% CPM respectively.

4 Discussions and Conclusions

Overall, 3D CT point clouds can be feasible data representations on nodule detection tasks for medical image analysis with a very careful data preprocessing. 3D point clouds naturally present the irregular shape of lung regions in real-world coordinates, which are flexible in employing multi-view features based on the geometric invariance and acquiring the discriminative spatial features from different viewpoints. Multi-view features can be obtained by rotating the 3D point clouds and further aggregated them to acquire the coarse nodule predictions through a nodule proposal optimization schema. By simultaneously learning the multi-view features from a 3D SparseConv encoder, combined with the multi-level and semantic segmentation features extracted from a 3D SparseConv decoder, the proposed nodule detector achieves a promising performance on the pulmonary nodule detection task.

The point cloud-based backbone network tends to extract informative spatial relations for nodule prediction. As small nodules contain few points, the lack of spatial feature extraction makes it challenging to detect. In contrast, the image-based methods handle it relatively well due to detailed texture information extracted from image-based CNNs at the low-level layers. There are still opportunities for further improvements on small nodule detection. Future work will extend the 3D point-cloud representations with image-based texture features detecting nodules via a dynamic multi-view nodule proposal optimization schema. It is worth investigating to fully utilize the spatial representations from 3D CT point clouds, which have the potential to benefit the clinical diagnosis, especially in surgical operations.

Acknowledgements. This work was supported in part by the National Science Foundation under award number IIS-2041307 and Memorial Sloan Kettering Cancer Center Support Grant/Core Grant P30 CA008748.

References

1. Aaa, S., et al.: Validation, comparison, and combination of algorithms for automatic detection of pulmonary nodules in computed tomography images: the LUNA16 challenge. *Med. Image Anal.* **42**, 1–13 (2017). [dataset]
2. Ahmed, S.M., Liang, P., Chew, C.M.: EPN: edge-aware PointNet for object recognition from multi-view 2.5 D point clouds. In: IROS, pp. 3445–3450 (2019)
3. Bandos, A.I., Rockette, H.E., Song, T., Gur, D.: Area under the free-response ROC curve (FROC) and a related summary index. *Biometrics* **65**(1), 247–256 (2009)
4. Chen, R., Han, S., Xu, J., Su, H.: Point-based multi-view stereo network. In: Proceedings of the IEEE/CVF International Conference on Computer Vision, pp. 1538–1547 (2019)
5. Ding, J., Li, A., Hu, Z., Wang, L.: Accurate pulmonary nodule detection in computed tomography images using deep convolutional neural networks. In: Descoteaux, M., Maier-Hein, L., Franz, A., Jannin, P., Collins, D.L., Duchesne, S. (eds.) MICCAI 2017. LNCS, vol. 10435, pp. 559–567. Springer, Cham (2017). https://doi.org/10.1007/978-3-319-66179-7_64
6. Dou, Q., Chen, H., Jin, Y., Lin, H., Qin, J., Heng, P.A.: Automated pulmonary nodule detection via 3D convnets with online sample filtering and hybrid-loss residual learning. In: International Conference on Medical Image Computing and Computer-Assisted Intervention, pp. 630–638 (2017)
7. Dou, Q., Chen, H., Yu, L., Qin, J., Heng, P.A.: Multilevel contextual 3-D CNNs for false positive reduction in pulmonary nodule detection. *IEEE Trans. Biomed. Eng.* **64**(7), 1558–1567 (2017)
8. Drokin, I., Ericheva, E.: Deep learning on point clouds for false positive reduction at nodule detection in chest CT scans. arXiv preprint [arXiv:2005.03654](https://arxiv.org/abs/2005.03654) (2020)
9. El-Regaily, S.A., Salem, M.A.M., Aziz, M.H.A., Roushdy, M.I.: Multi-view convolutional neural network for lung nodule false positive reduction. *Expert Syst. Appl.* **162**, 113017 (2020)
10. Gong, Z., Li, D., Lin, J., Zhang, Y., Lam, K.M.: Towards accurate pulmonary nodule detection by representing nodules as points with high-resolution network. *IEEE Access* **8**, 157391–157402 (2020)
11. Gupta, A., Saar, T., Martens, O., Moullec, Y.L.: Automatic detection of multi-size pulmonary nodules in CT images: large-scale validation of the false-positive reduction step. *Med. Phys.* **45**(3), 1135–1149 (2018)
12. Han, Z., Wang, X., Liu, Y.S., Zwicker, M.: Multi-angle point cloud-VAE: unsupervised feature learning for 3D point clouds from multiple angles by joint self-reconstruction and half-to-half prediction. In: 2019 IEEE/CVF International Conference on Computer Vision (ICCV), pp. 10441–10450. IEEE (2019)
13. Khosravan, N., Bagci, U.: S4ND: single-shot single-scale lung nodule detection. In: International Conference on Medical Image Computing and Computer-Assisted Intervention, pp. 794–802 (2018)
14. Kim, B.C., Yoon, J.S., Choi, J.S., Suk, H.I.: Multi-scale gradual integration CNN for false positive reduction in pulmonary nodule detection. *Neural Netw.* (2019)

15. Li, Y., Fan, Y.: DeepSEED: 3D squeeze-and-excitation encoder-decoder convolutional neural networks for pulmonary nodule detection. In: 2020 IEEE 17th International Symposium on Biomedical Imaging (ISBI), pp. 1866–1869. IEEE (2020)
16. Li, Z., Zhang, S., Zhang, J., Huang, K., Wang, Y., Yu, Y.: MVP-Net: multi-view FPN with position-aware attention for deep universal lesion detection. In: Shen, D., et al. (eds.) MICCAI 2019. LNCS, vol. 11769, pp. 13–21. Springer, Cham (2019). https://doi.org/10.1007/978-3-030-32226-7_2
17. Liu, J., Cao, L., Akin, O., Tian, Y.: 3DFPN-HS²: 3D feature pyramid network based high sensitivity and specificity pulmonary nodule detection. In: Shen, D., et al. (eds.) MICCAI 2019. LNCS, vol. 11769, pp. 513–521. Springer, Cham (2019). https://doi.org/10.1007/978-3-030-32226-7_57
18. Liu, J., Cao, L., Akin, O., Tian, Y.: Accurate and robust pulmonary nodule detection by 3D feature pyramid network with self-supervised feature learning. arXiv preprint [arXiv:1907.11704](https://arxiv.org/abs/1907.11704) (2019)
19. Phan, A.V., Le Nguyen, M., Nguyen, Y.L.H., Bui, L.T.: DGCNN: a convolutional neural network over large-scale labeled graphs. *Neural Netw.* **108**, 533–543 (2018)
20. Qi, C.R., Su, H., Mo, K., Guibas, L.J.: PointNet: deep learning on point sets for 3D classification and segmentation. In: Proceedings of the IEEE Conference on Computer Vision and Pattern Recognition, pp. 652–660 (2017)
21. Qi, C.R., Yi, L., Su, H., Guibas, L.J.: PointNet++: deep hierarchical feature learning on point sets in a metric space. In: Advances in Neural Information Processing Systems, pp. 5099–5108 (2017)
22. Setio, A.A.A., et al.: Pulmonary nodule detection in CT images: false positive reduction using multi-view convolutional networks. *IEEE Trans. Med. Imaging* **35**(5), 1160–1169 (2016). <https://doi.org/10.1109/TMI.2016.2536809>
23. Setio, A.A.A., et al.: Pulmonary nodule detection in CT images: false positive reduction using multi-view convolutional networks. *IEEE Trans. Med. Imaging* **35**(5), 1160–1169 (2016)
24. Shi, S., et al.: PV-RCNN: point-voxel feature set abstraction for 3D object detection. In: Proceedings of the IEEE/CVF Conference on Computer Vision and Pattern Recognition, pp. 10529–10538 (2020)
25. Shi, S., Wang, Z., Shi, J., Wang, X., Li, H.: From points to parts: 3D object detection from point cloud with part-aware and part-aggregation network. *IEEE Trans. Pattern Anal. Mach. Intell.* (2020)
26. Siegel, R.L., Miller, K.D., Jemal, A.: Cancer statistics, 2019. *CA Cancer J. Clin.* **69**(1), 7–34 (2019)
27. Team, O.D.: OpenPCDet: an open-source toolbox for 3D object detection from point clouds (2020). <https://github.com/open-mmlab/OpenPCDet>
28. Usman, M., Lee, B.D., Byon, S.S., Kim, S.H., Lee, B.i., Shin, Y.G.: Volumetric lung nodule segmentation using adaptive ROI with multi-view residual learning. *Sci. Rep.* **10**(1), 1–15 (2020)
29. Wang, B., Qi, G., Tang, S., Zhang, L., Deng, L., Zhang, Y.: Automated pulmonary nodule detection: high sensitivity with few candidates. In: Frangi, A.F., Schnabel, J.A., Davatzikos, C., Alberola-López, C., Fichtinger, G. (eds.) MICCAI 2018. LNCS, vol. 11071, pp. 759–767. Springer, Cham (2018). https://doi.org/10.1007/978-3-030-00934-2_84

30. Zanjani, F.G., Moin, D.A., Verheij, B., Claessen, F., Cherici, T., Tan, T., et al.: Deep learning approach to semantic segmentation in 3D point cloud intra-oral scans of teeth. In: International Conference on Medical Imaging with Deep Learning, pp. 557–571 (2019)
31. Zhu, W., Liu, C., Fan, W., Xie, X.: DeepLung: deep 3D dual path nets for automated pulmonary nodule detection and classification. In: 2018 IEEE Winter Conference on Applications of Computer Vision (WACV), pp. 673–681 (2018)